ACS OMEGA

http://pubs.acs.org/journal/acsodf

Article

Multistage Gradient Bioinspired Riblets for Synergistic Drag Reduction and Efficient Antifouling

Xianxian Cui, Dengke Chen, and Huawei Chen*

Cite This: *ACS Omega* 2023, 8, 8569−8581

Read Online

ACCESS | Metrics & More | Article Recommendations | Supporting Information

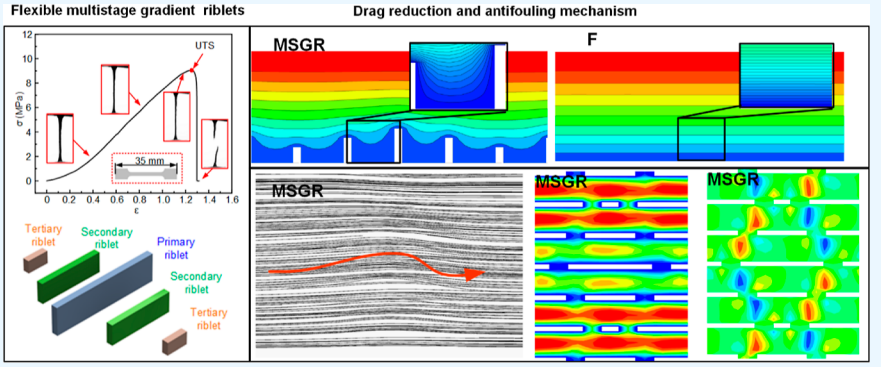

ABSTRACT: Shark skin-inspired riblets have represented the tremendous potential for drag reduction (DR) and antifouling in submarine, ship, and so on. Most studies simplified the complex denticle embedded in the shark skin into the single-stage riblet with uniform parameters, ignoring the influence of riblet height gradient and material deformation on DR and antifouling. In the present study, flexible multistage gradient riblets (MSGRs) with varied heights were proposed, and their DR and antifouling effects were investigated by the experiment and numerical simulation. The experimental results showed that the maximum DR rate of flexible MSGRs with an elastic modulus of 4.592 MPa could reach 16.8% at a flow velocity of 0.5 m/s. Moreover, the dynamic adhesion measurement indicated a reduction by 69.6% of the adhesion area of *Chlorella vulgaris* on the flexible MSGR surface. The results identified that flexible MSGRs with low surface energy could generate steady high- and low-velocity streaks and alter the flow state of the fluid, thus lessening the average velocity gradient near the wall and the adhering selectivity of pollutants in riblet and achieving synergistic DR and efficient antifouling. Taken together, the proposed flexible MSGR surface holds promise for reducing surface friction and inhibiting particle attachment in engineering applications.

1. INTRODUCTION

Drag reduction (DR) and antifouling have been plaguing various industries. For instance, over 50% of fuel consumption in ships is attributed to surface drag.[1] Moreover, the surface fouling on the underwater ships is also severe and inevitable, usually intensifying the drag. Generally, as the fouling coverage rate was 5%, the ship drag was twice greater than that of the clean surface, and the fuel consumption increased by 10%. Therefore, it was beneficial to design the composite surface with DR and antifouling abilities.[2] Natural creatures evolving unique structures and excellent surface functions through millions of years of natural selection could adapt to the harshest environment.[3−9] Inspired by natural creatures, scientists and engineers have obtained many innovative inspirations to address the above technical challenges.[10−12] Numerous studies have indicated that many tiny denticles embedded in the shark skin and parallel to the streamwise direction played a decisive role in reducing drag and antifouling.[13−16]

However, due to the complexity of the denticle structure, it was intractable to fabricate the real shark skin surface in a large area, and thus, scientists generally simplified the denticle into riblet structures with triangular, rectangular, and other cross-sections.[17−20] Schumacher et al.[21] prepared a new type of environment-friendly ship coating named barnacle-specific Sharklet AF based on the micro-topographical characteristics of shark skin. Dai et al.[22] developed the shark-skin-like surface with a 90° orientation by three-dimensional (3D) printing and accessed its DR effect with a rheometer. Qin et al.[23] modified the bionic non-smooth surface by combining ZIF-67 particles to enhance its DR and antifouling properties. Zhou et al.[20,24]

Received: December 4, 2022
Accepted: February 7, 2023
Published: February 20, 2023

https://doi.org/10.1021/acsomega.2c07729
ACS Omega 2023, 8, 8569−8581

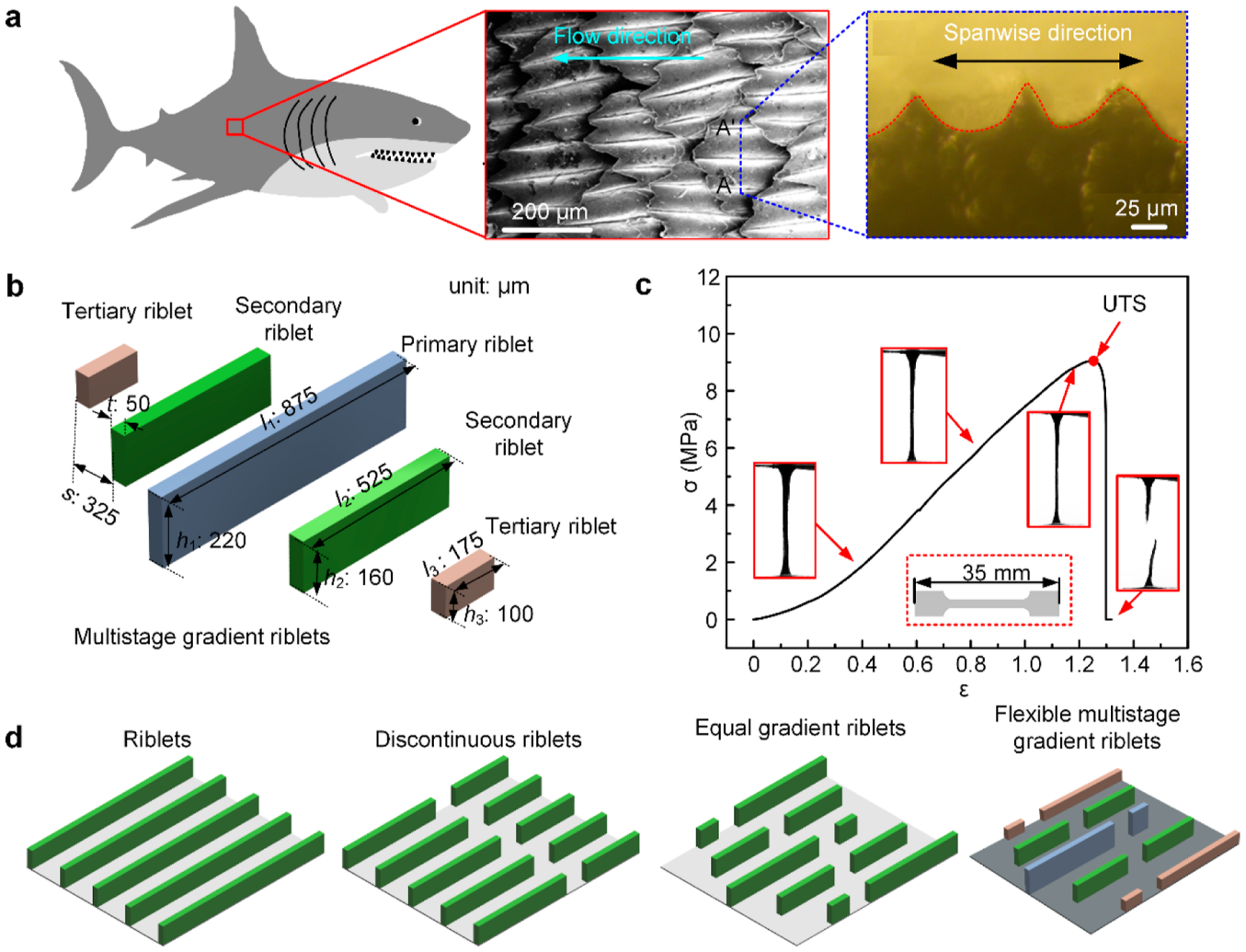

Figure 1. Shark skin shield scale model construction. (a) Schematic diagram of shark and SEM image of shark skin. Photograph courtesy of Huawei Chen, Xin Zhang, Lingxi Ma, Da Che, Deyuan Zhang, and T.S. Sudarshan. Copyright 2014. (b) Simplified shield scale structure. (c) Stress−strain curve of shark skin in the hydrated state. (d) Conceptual model of various patterned surfaces: riblets (Rs), discontinuous riblets (DCRs), equal gradient riblets (EGRs), and flexible MSGRs.

fabricated multilayer hierarchical riblets by three-layer hybrid mask lithography, which presented an excellent air DR. Additionally, shark skin has an excellent antifouling effect.[20,22,25,26] Chung et al.[27] and Schumacher et al.[21] found that Sharklet AF based on the shark skin had a significant antifouling effect on *Staphylococcus aureus* and zoospores of *Ulva linza*. Choi et al.[28] and Yoo et al.[29] investigated the influence of the spacing dimension of the Sharklet structure on membrane biofouling and observed that the 2 μm spaced pattern exhibited the least fouling. Lee et al.[30] and Schumacher et al.[31] found that the increasing length gradient of the riblet on the bionic shark skin surface was beneficial in reducing the residence time of pollutant particles on the patterned surface. It can be seen that the application of bionic shark skin structure with changing parameters has been a new trend for DR and antifouling. Therefore, it is significant to further study the comprehensive effect of bionic shark skin structure with changing heights in response to DR and antifouling. In addition, DR and antifouling are a complicated subject related not only to the surface morphology of bionic shark skin structure but also to wettability, surface free energy, surface roughness, and mechanical properties.[32,33]

In this paper, considering the height gradient of the shark skin shield scale structure, five bionic flexible multistage gradient riblet (MSGR) surfaces with different mechanical properties were prepared by polydimethylsiloxane (PDMS). To analyze the DR and antifouling effects of the prepared flexible MSGR surface, it was compared with MSGR surfaces and classic single-stage riblet surfaces. Surface drag and fouling were determined using a closed water tunnel and *Chlorella vulgaris* coloring tests, respectively. Moreover, numerical evaluation was performed on the flow characteristics of the bionic surface; the influence of the bionic surface on the near-wall flow field was analyzed; the pollutant pathway was determined by numerical simulation; the effects of wettability on DR and antifouling were evaluated by dynamic and static contact angles (CAs) and surface free energy; and the possible new DR and antifouling mechanisms of the flexible MSGR surface were studied. In addition, in terms of the DR and antifouling, the flexible MSGR surface inspired by shark skin not only showed great application potential in underwater vehicles but also enlightened the reasons for other similar flexible gradient structures by exploring its internal mechanism.

https://doi.org/10.1021/acsomega.2c07729
ACS Omega 2023, 8, 8569−8581

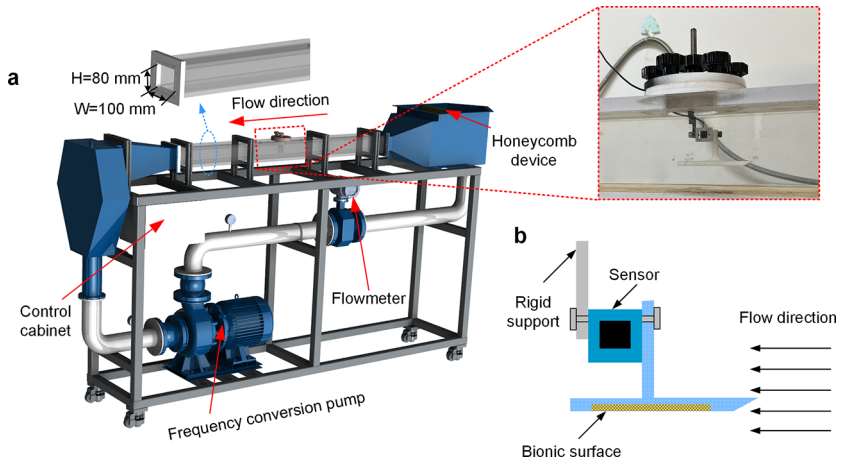

Figure 2. Schematic diagram of the closed circulating water tunnel. (a) 3D diagram, with the red dotted box showing the physical diagram of the bionic surface installation. (b) Schematic diagram of the bionic surface and stress−strain sensor installation.

2. METHODS

2.1. Establishment of the Flexible MSGR Model. Early members of our laboratory used scanning electron microscopy (SEM) to observe epidermis samples from the abdomen of gray whale sharks.[11,12,34] The surface of the shark skin was geometrically non-smooth and covered with many tiny denticles, as shown in Figure 1a. For a single denticle, the length and height of the riblet decreased from the middle to both sides, presenting a multistage gradient distribution, and this main feature formed the basis of the MSGR design. Considering the limitations of experiments and fabrication processes, the designed MSGRs were simplified into three-stage gradient riblets. The length of the primary, secondary, and tertiary riblets was obtained by multiplying the average of the scale characteristic dimensions by 3, with the corresponding size parameters shown in Figure 1b. Based on the dimensionless unit of the riblet spacing $s^+ \approx 15$ and test conditions, the riblet spacing (s) of all experimental samples was 325 μm. The denticle embedded in the flexible dermis layer can move in real time. Therefore, it is necessary to analyze the mechanical properties of shark skin in the hydrated state to study the DR and antifouling mechanism of real sharks. According to the stress−strain curve obtained from the tensile test in Figure 1c, the elastic modulus and tensile strength of shark skin were 4.096 and 9.544 MPa, respectively. Based on the mechanical properties of shark skin and the simplified scale structure, a flexible MSGR surface was established.

To verify the DR and antifouling effect of flexible MSGRs, several classic single-stage riblets with uniform height, that is, R, DCR, and EGR surfaces, were designed, as illustrated in Figure 1d. As can be seen, all riblets were rectangular parallelepipeds with a width of 50 μm. The heights of all riblets except for flexible MSGRs were 160 μm. In flexible MSGRs, the heights of the primary, secondary, and tertiary riblets were 220, 160, and 100 μm, respectively. The EGR and flexible MSGR surfaces comprised five riblets of different length scales within one rhombus-shaped pattern. The longest riblet in the design was 875 μm in length in the middle, and the other riblets with lengths of 525 and 175 μm were symmetrically positioned on both sides. In R and DCR surfaces, the lengths of a single riblet were infinite and 875 μm, respectively.

2.2. Fabrication of Samples. Compared with traditional milling and molding, 3D printing was easy and cost-effective in generating surfaces with shark skin textures.[22,35] This study fabricated all rigid bionic patterned surfaces using a 3D printer (nanoArch P150) with an optical resolution of 25 μm. The printing materials were high-temperature-resistant resins with an elastic modulus of 4.2 GPa, and printing was performed at room temperature. The ultraviolet exposure time was 1 s, with an intensity of 150 lx. The thickness of each layer was 10 μm, and the delay time for the platform to stay after descent was 2 s. The length and width of all printed bionic surfaces were 39 and 24 mm, respectively. In addition, the flat (F) surface was also printed for comparison. Five flexible MSGR surfaces with different elastic moduli were prepared by the PDMS replica molding method, and the preparation process is shown in Figure S1.

2.3. Wetting Properties. The values of static and dynamic CAs with 2 μL of ultrapure water droplets on various surfaces were evaluated by a CA meter (OCA25, Beijing Audreno Instrument Co., Ltd., China). The surface free energy γ_s of all substrates was evaluated by the Owens−Wendt−Rabel−Kaelble method via measuring the static CA using two polar liquids, water and ethanol. Due to the anisotropic pattern of the bionic patterned surface, the static CAs of all surfaces were measured in the directions parallel and perpendicular to the surface.

2.4. DR Evaluation of the Flexible MSGR Surface. A closed circulating water tunnel was used to evaluate the DR performance of the flexible MSGR surface, as shown in Figure 2a. The prepared flexible MSGR surface was placed in the groove of the mold, and the direction of flexible MSGR was parallel to the flow direction. The total length of the test section made of transparent acrylic acid was 1500 mm, and the mold was placed in the middle of the test section. All flexible MSGR surfaces were tested at different flow velocities (0.5, 1, 1.5, 2, and 2.5 m/s). The Reynolds number ($Re = \rho U_\infty d/\mu$, where ρ is the water density, U_∞ is the flow velocity, d is the hydraulic diameter of the test section, and μ is the dynamic viscosity) was much greater than 4000 at the flow velocity of 0.5 m/s, indicating the turbulent flow.[36] Figure 2b shows the drag measuring device of the flexible MSGR surface in the circulating water tunnel. The stress−strain sensor is a unidirectional force device with an accuracy of 0.01 mN and a measuring range of 0−50 N and is used for measuring the

https://doi.org/10.1021/acsomega.2c07729
ACS Omega 2023, 8, 8569−8581

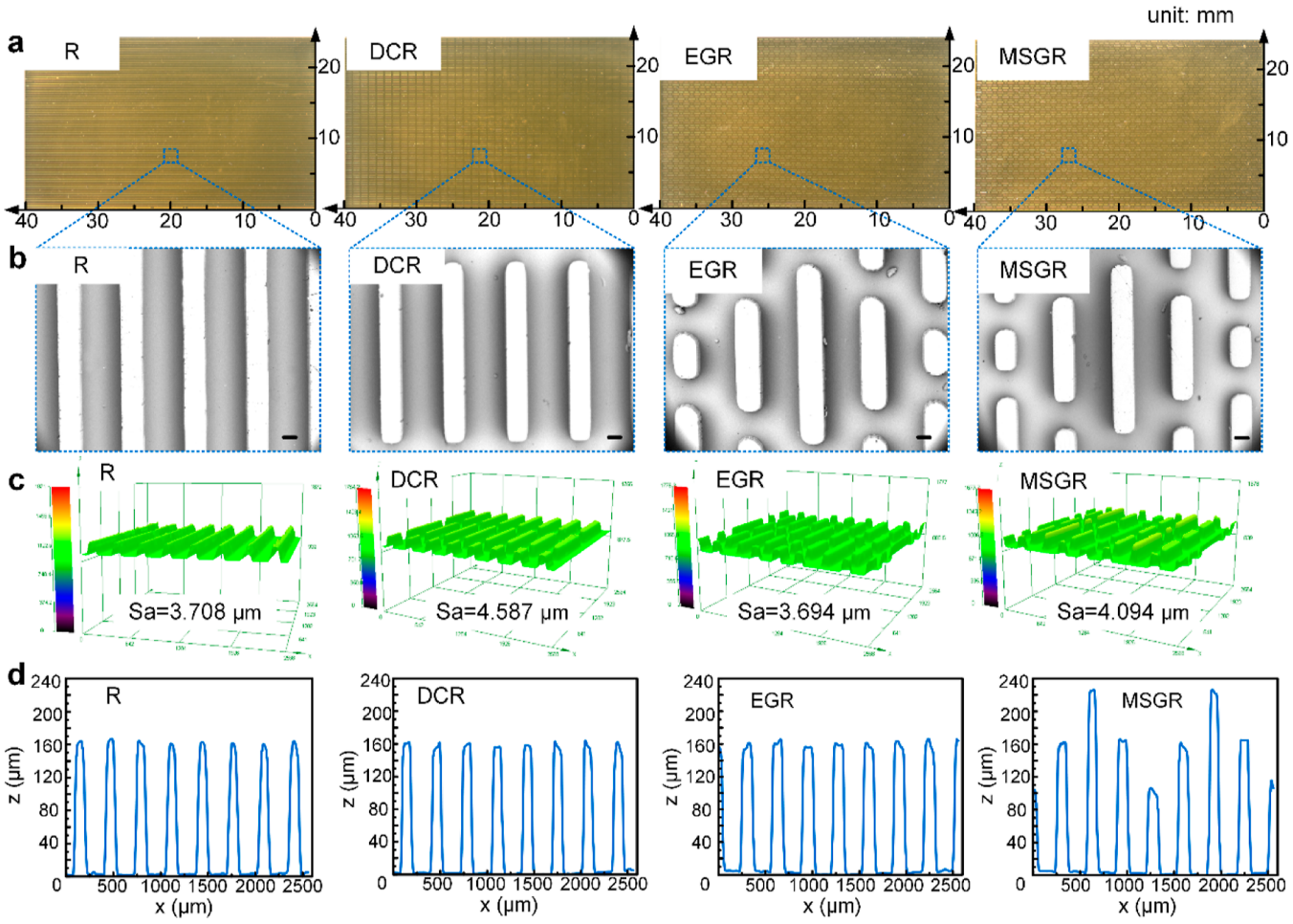

Figure 3. Morphology of four different bionic surfaces. (a) Optical images, (b) SEM images, (c) 3D topographical images, and (d) z profile of the fabricated surfaces. Scale bars: 100 μm.

total drag. The drag of flat surfaces and other rigid bionic patterned surfaces was measured to evaluate the DR effect of flexible MSGR surfaces. Before the experiment, the sensor should be calibrated, and the evaluated error should be controlled within ±0.02 mN to ensure the accuracy of each experiment.

2.5. Antifouling Evaluation of the Flexible MSGR Surface. *C. vulgaris* (Nanjing Haiersi Biotechnology Co., Ltd., China) was selected to evaluate the antifouling performance of bionic surfaces. Artificial seawater without heavy metals and with 24‰ salinity was prepared according to ASTM D1141-98 (2013). The culture container and the prepared sample were sterilized at 120 °C for 30 min. Subsequently, the sample was immersed in *C. vulgaris* solution which was placed in a homeothermic double-layer oscillation incubator (HZQ-X 100, Suzhou Pei Ying Experimental Equipment Co., Ltd.) to test the antifouling effect under dynamic water flow. By shaking the culture container, the solution was disturbed to simulate the water flow in the real environment.

The samples were cultured at 20−28 °C under sufficient light conditions for 21 d. Then, the non-adsorbed *C. vulgaris* on bionic surfaces was washed away by deionized water. An intuitive observation method was carried out to evaluate the antifouling effect of the surface, during which four observation points were randomly selected on the surface for quantitative analysis using an optical microscope. To visually observe the antifouling performance of the flexible MSGR surface, a certain amount of coffee solution was dripped on different bionic surfaces to observe the rolling of coffee droplets at different inclination angles.

2.6. Simulation of Flow Fields around the Flexible MSGR Surface. To explore the DR and antifouling mechanisms of the flexible MSGR surface and rigid bionic surfaces, the isothermal and 3D flow of fluids on various surfaces were numerically simulated using Ansys Fluent software under the experimental turbulent flow conditions. The flat surface (upper surface) and the bionic patterned surface (bottom surface) were placed in the same calculation domain for comparison, which was convenient for analyzing the DR effect of the bionic surface. The calculation model is shown in Figure S2a. The x, y, and z directions of the flow field corresponded to the spanwise direction, flow direction, and longitudinal direction of the model, respectively. The mesh size of the model decreased from the wall by 1.2 equal proportion. The height of the first layer of the mesh from the wall was 1×10^{-6} m, which could meet the requirements of large eddy simulation (LES) on the accuracy of the mesh, as shown in Figure S2b. In addition, grid independence was verified, and the average grid quality index confirmed the excellent construction of elements in each case. Translational periodic boundary conditions were utilized on the inlet and outlet of the computational domain to ensure the fully developed flow, and the inlet velocity (U_∞ = 1 m/s) was applied to the entire channel. Symmetric boundary conditions were adopted on

https://doi.org/10.1021/acsomega.2c07729
ACS Omega 2023, 8, 8569−8581

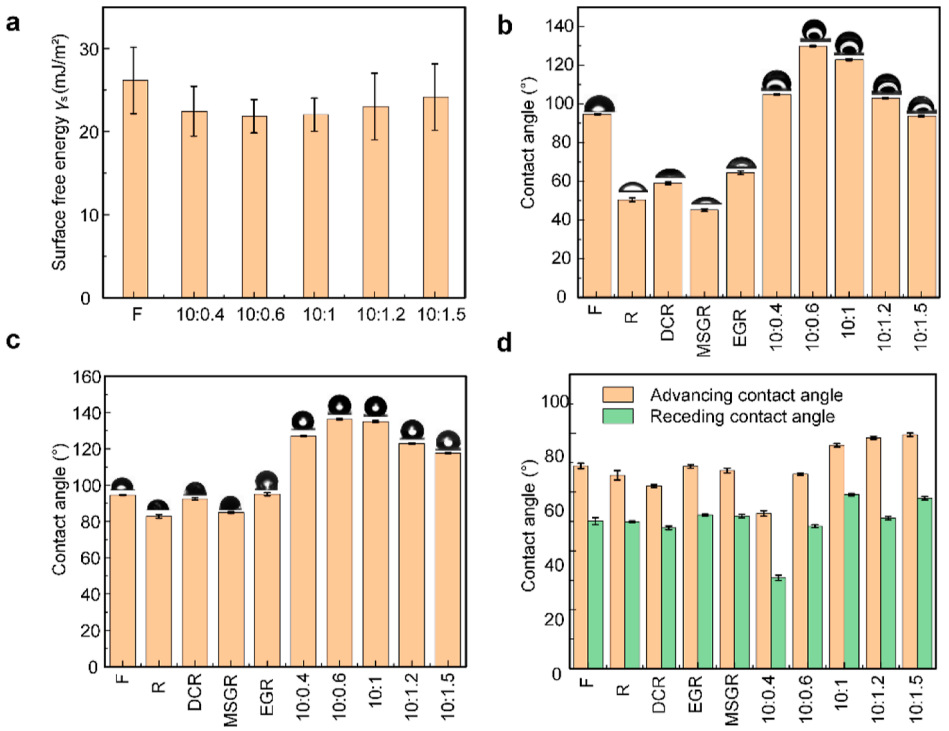

Figure 4. Wetting properties of different surfaces. (a) Surface free energy γ_s of different materials. (b) Static CAs of different bionic surfaces in the parallel direction. (c) Static CAs of different bionic surfaces in the perpendicular direction. (d) Advancing and receding angles of different bionic surfaces.

both side walls. When fluid−solid coupling was not considered, no-slip conditions were set at the bottom surface. When the fluid−solid coupling was considered, a coupling interface was set at the bottom surface. In the computational fluid dynamics analysis, water was chosen as the fluid medium. First, the steady flow field was calculated by the re-normalization group (RNG) $k-\varepsilon$ turbulence model, which provided the initial field for transient calculation. On this basis, the flow field characteristics were analyzed using the LES method and the wall-adapting local eddy-viscosity subgrid-scale model. In addition, the pressure−velocity coupling was modified by the pressure-implicit with splitting of operators algorithm. The momentum equation was discretized by bounded central differencing, and the time term was solved by a second-order implicit method to obtain higher accuracy. When the residual values of continuity, x-velocity, y-velocity, and z-velocity were less than 1×10^{-8}, the solution was assumed to be convergent.

3. RESULTS

3.1. Microstructure of MSGRs. Figure 3a shows the optical images of the printed three classic single-stage riblets and MSGRs, and Figure 3b shows partially enlarged SEM images. It can be seen that the designed structure was precisely printed, and the straightness of the riblet edges was well maintained. The surface topography of the fabricated samples was measured by an atomic force laser confocal microscope (OLS4500, Olympus Corporation, Japan), as shown in Figure 3c,d. All fabricated samples had a surface roughness of less than 5 μm and an average height of 163.5 μm, with an error of 2.2% compared to the design height of 160 μm.

3.2. Wetting Properties of Flat and Bionic Patterned Surfaces. The surface free energy γ_s is the work required to increase the surface area of a solid, and γ_s of a solid is closely related to its wettability. Higher γ_s values indicate that the surface is easier to wet, and the static CA is smaller.[37] Therefore, F was the most wettable substrate in this paper, which was consistent with the measured small static CA (94.5 ± 0.3°), as shown in Figure 4a. The PDMS substrates with different elastic moduli showed similar γ_s values (close to 20 mJ/m^2) and low surface free energy, which made these substrates less wettable. In addition, the wettability of all polymers is affected by the micro-morphology. As shown in Figure 4b,c, R, DCR, EGR, and MSGR surfaces showed greater hydrophilicity than the F surface. This phenomenon was more pronounced in the parallel direction than that in the perpendicular direction. PDMS with different elastic moduli showed similar hydrophobicity in the perpendicular direction. However, PDMS with a ratio of 10:0.6 in the parallel direction exhibited slightly higher hydrophobicity, and the smooth substrates also showed similar behavior. The difference between the advancing angle and the receding angle is CA hysteresis, which can be directly reflected by the sliding angle, as shown in Figure S3. For flexible MSGR surfaces, PDMS with a ratio of 10:1 had the smallest sliding angle, indicating that droplets rolled off the surface easily, as shown in Figure 4d. For marine DR and antifouling research, the surface to be analyzed needs to be immersed in a liquid medium.[37] In this case, only describing the wetting properties in the air cannot provide enough details about the surface properties, but it may help detect the dynamic behavior of the surface.

3.3. DR Effect Analysis. The drag data of each surface were measured by the circulating water tunnel, and the collected drag data were averaged to obtain the average drag of each surface at different flow velocities. Figure 5a shows the drag of the flat at different flow velocities. In addition, three experiments were conducted for each measurement, and the average was taken as the final value of the measurement. A

https://doi.org/10.1021/acsomega.2c07729
ACS Omega 2023, 8, 8569−8581

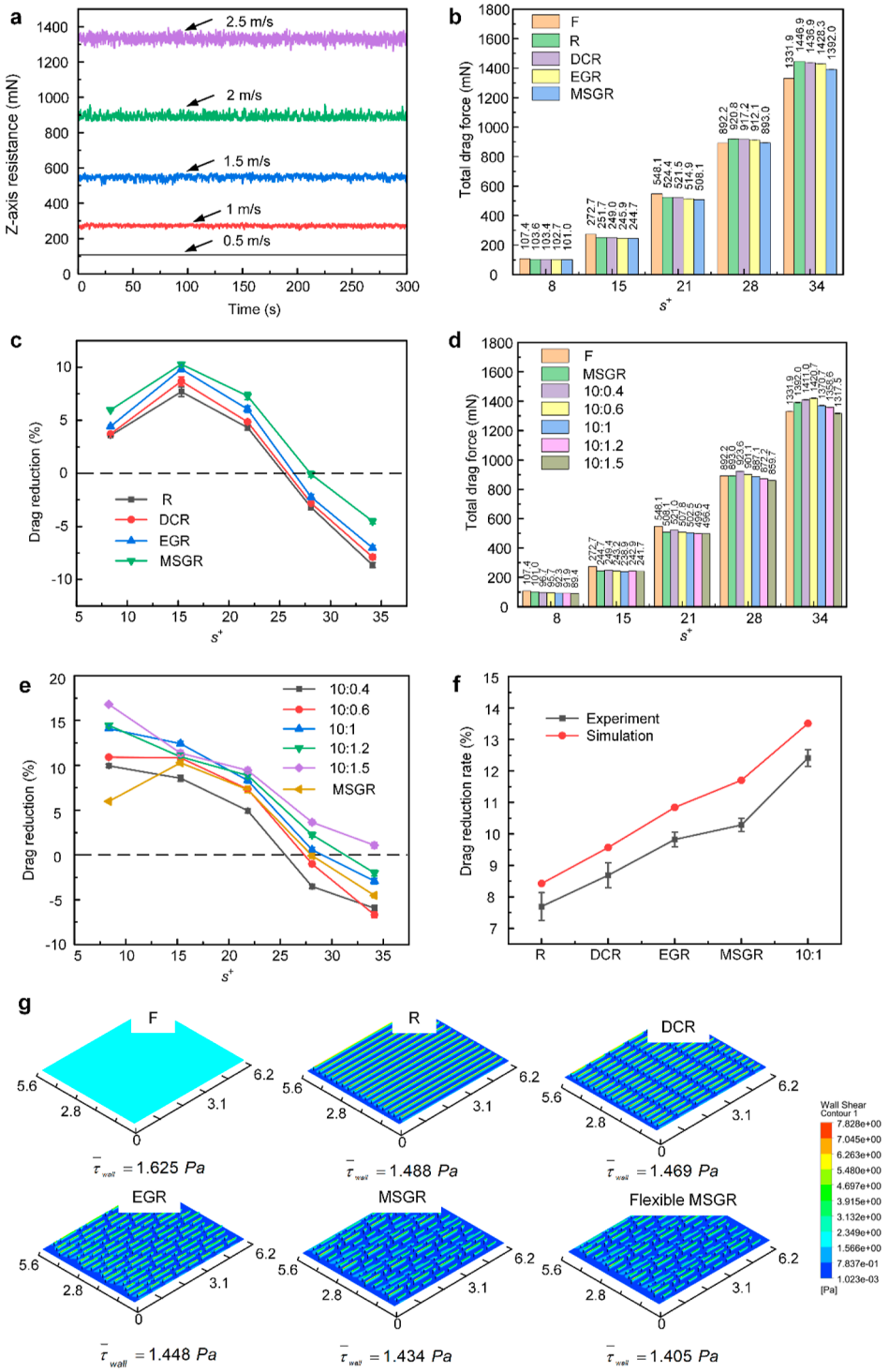

Figure 5. DR effects on different surfaces. (a) Drag of the F surface. (b) Average drag of the rigid bionic surface. (c) DR rate of the rigid bionic surface. (d) Drag of the flexible MSGR surface. (e) DR rate of the flexible MSGR surface. (f) Simulation reliability verification. (g) Wall shear stress distribution of the R, DCR, EGR, MSGR, and flexible MSGR surfaces was compared with that of the F surface, where the flexible MSGR surface was made of PDMS and curing agent in the ratio of 10:1.

confidence interval of 0.95 was taken as the error bar of the measurement. Figure 5b shows the average drag measured on the F surface, the MSGR surface, and three classic single-stage riblet surfaces. The drag was proportional to the flow velocity, and the drag of bionic patterned surfaces was smaller than that of the F surface under the same test conditions when s^+ was within 8−21. To quantitatively analyze the DR effect of the bionic surface, the relative DR rate was calculated as follows

$$\mathrm{DR}\,(\%) = \frac{F_{\mathrm{flat}} - F_{\mathrm{bionic}}}{F_{\mathrm{flat}}} \times 100\% \tag{1}$$

where F_{flat} and F_{bionic} denoted the drag force of the F surface and the bionic surface, respectively.

The dimensionless spacing s^+ value varies with velocity, and the DR rate can be compared among different surfaces for a given s^+ value. As shown in Figure 5c, all bionic surfaces

https://doi.org/10.1021/acsomega.2c07729
ACS Omega 2023, 8, 8569−8581

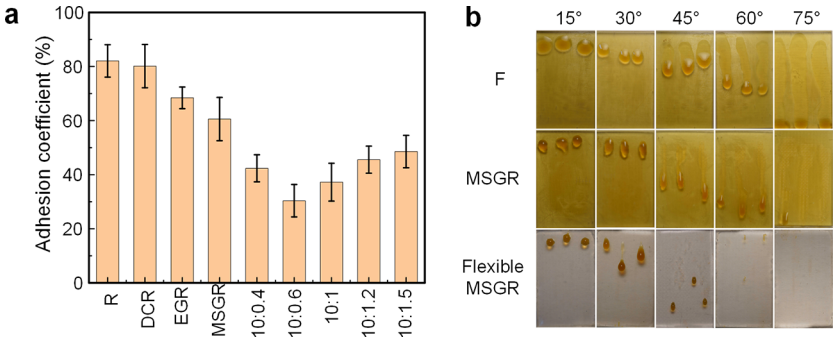

Figure 6. *C. vulgaris* attachment on different surfaces. (a) Adhesion coefficient. (b) Change of coffee droplets on different material surfaces with inclination angles, where the flexible MSGR surface was made of PDMS and curing agent in the ratio of 10:1.

exhibited an excellent DR effect, and the DR rate first increased and then decreased with the ascending s^+ values. It should be noted that the DR rate varied with the surface structure. Over the entire test range, the MSGR surface had the highest DR rate of about 10.3%, followed by the EGR surface. The maximum DR rate of EGR and MSGR surfaces was very close. However, when the s^+ value exceeded 15, the DR rate of three classic single-stage riblet surfaces decreased rapidly; when the s^+ value reached 27, EGR reached the state of increasing drag, while MSGR still maintained the DR state. The results showed that the MSGR surface could achieve DR over a wide velocity range compared with other single-stage riblet surfaces, expanding the effective DR velocity range.

To study the DR effect of the coupling of flexibility and denticle, boundary conditions and material properties were set to allow the flexible riblet to deform under the action of fluid shear. The water tunnel was used to calculate the surface drag of flexible MSGR with different elastic moduli, and the DR effect with different s^+ values was obtained, as shown in Figure 5d,e. With the increasing s^+ value, the DR rate tended to decrease. Even at a high s^+ value, the DR effect of some flexible surfaces was inhibited. Generally speaking, the DR effect of the flexible MSGR surface was better than that of the rigid MSGR surface. The maximum DR rate of the flexible surface with a ratio of 10:1.5 could reach 16.8%. Even when the s^+ value was 35, there was still a DR effect. According to the literature, the elastic modulus was 0.219, 0.941, 2.22, 3.114, and 4.592 MPa when the ratio of PDMS to the curing agent was 10:0.4, 10:0.6, 10:1, 10:1.2, and 10:1.5, respectively.[38] Therefore, it was not difficult to conclude that the maximum DR rate first increased and then decreased as the elastic modulus increased, and the elastic modulus of shark skin was close to the optimal DR elastic modulus.

To investigate the reasons for the difference in the DR performance of different bionic patterned surfaces, the flow field around different bionic patterned surfaces was analyzed. In addition, the simulation reliability was verified under the simulation setting. As shown in Figure 5f, the simulation values agreed well with the experimental values, indicating that the simulation model was reliable. Significantly, the experimental results were a little lower than those of the simulated one, which might be attributed to the difference in the machining precision of the surface microstructure of the bionic sample and the numerical simulation model. Figure 5g shows the wall shear stress distribution of different bionic patterned surfaces. Note that the same legend was used to represent different situations for ease of comparison. Obviously, almost no extreme shear stress was observed for an F surface, such as the maximum and minimum values in the legend. For the bionic surface, the riblet tip and the top half of the riblet sidewall presented relatively high wall shear stress, even reaching the maximum value in some places. However, the wall shear stress in most areas of the valley and riblet sidewalls was far less than that of the F surface, resulting in a lower total average shear stress than that of the F surface. Notably, fewer areas with higher shear stress were found near the riblet tip of the flexible MSGR surface, and more areas with lower shear stress existed in the valley, leading to the minimum total average shear stress of the flexible MSGR surface. This indicated that flexible MSGRs with height gradient structure could sufficiently reduce the shear stress and achieve an excellent DR effect.

3.4. Antifouling Performance. Two main reasons explained why fouling was often observed on the bottom and sidewalls of bionic surfaces. First, microorganisms naturally preferred the lower surface without additional external force. Second, fouling was affected by the shear stress level of the upper and lower walls under dynamic flow.[39] According to Figure 5g, the surface averaged wall shear stress on the top wall was considerably higher than that on the bottom wall, and a relatively minimal but significant difference in shear stress for different bionic surfaces was observed. Therefore, it was necessary to analyze the antifouling effect of different bionic surfaces, and this paper used the adhesion coefficient to evaluate the antifouling ability of different bionic surfaces, as expressed in eq 2.

$$A\ (\%) = \frac{N_i}{N_j} \times 100\% \tag{2}$$

where N_i was the adhesion area of *C. vulgaris* to different bionic surfaces per unit area, while N_j was the adhesion area of *C. vulgaris* to the F surface per unit area.

ImageJ software was employed to convert the images of the antifouling test results into the binary format, and the adhesion area was determined by the ratio of the black area (indicating *C. vulgaris* attachment) to the total area. Figure 6a shows the adhesion coefficient of *C. vulgaris* on different bionic surfaces. A confidence interval of 0.95 was taken as the error bar of the measurement. Compared with that on the F surface, the adhesion coefficient of *C. vulgaris* on different bionic surfaces was significantly declined. The adhesion coefficient decreased by ~32 and ~39% on the EGR surface and MSGR surface, respectively. The adhesion coefficient of *C. vulgaris* further reduced on the flexible MSGR surface, and the adhesion coefficient of *C. vulgaris* on the flexible MSGR surface with a

https://doi.org/10.1021/acsomega.2c07729
ACS Omega 2023, 8, 8569−8581

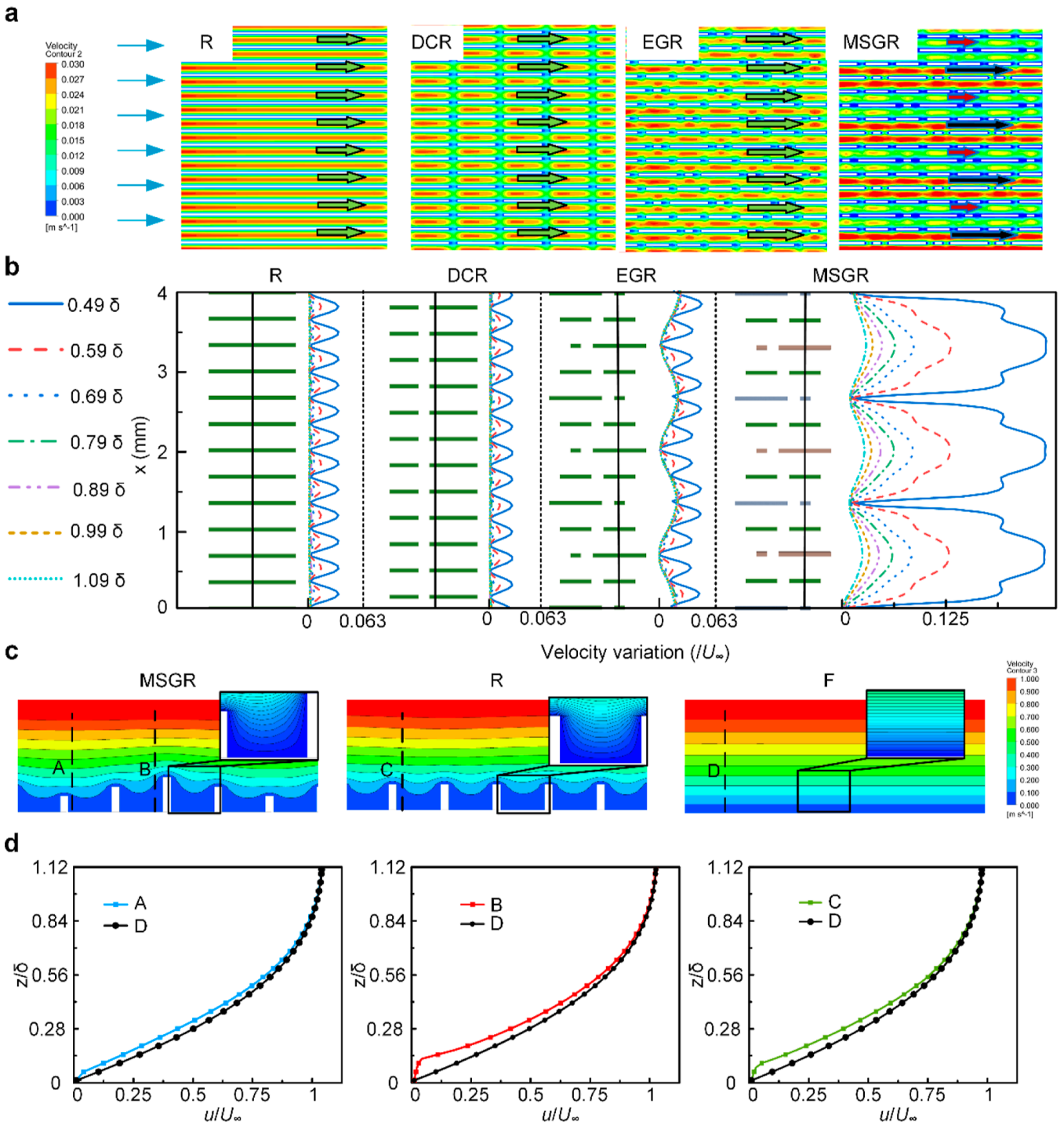

Figure 7. Velocity contours and velocity profiles on different bionic surfaces. (a) Velocity contours of R, DCR, EGR, and MSGR surfaces at a distance of $z = 0.1\delta$ from the bottom in a wall-parallel plane. The flow direction is indicated by arrows. Note that the blue arrows are consistent in length at the inlet, the lengths of the red and black arrows at the outlet are different at the MSGR surface, and the green arrows are uniform in the other cases. (b) Velocity variation of R, DCR, EGR, and MSGR in the spanwise direction at different wall-normal distances in the boundary layer. The black line indicates a position in the y-direction at a distance of 3100 μm from the inlet. (c) Velocity contours of MSGR, R, and F surfaces in the $x-z$ plane at a distance of 3100 μm from the inlet. (d) Velocity profile in the groove region corresponding to (c).

ratio of 10:0.6 decreased by nearly 69.6%. Moreover, the adhesion coefficient of *C. vulgaris* was slightly lower on the DCR surface than that on the R surface. As shown in Figure S4, *C. vulgaris* uniformly adhered to the F surface, with a significantly higher adhesion density than that of the bionic surface. Note that the lowest adhesion density of *C. vulgaris* was found on the riblet structure on the bionic surface. Overall, the adhesion coefficient and the number of *C. vulgaris* decreased significantly on the MSGR surface and flexible MSGR surface.

Figure 6b illustrates the antifouling performance of the MSGR surface and flexible MSGR surface. When the inclination angle increased from 15 to 30°, coffee droplets on all surfaces began to roll, with different rolling patterns

https://doi.org/10.1021/acsomega.2c07729
ACS Omega 2023, 8, 8569−8581

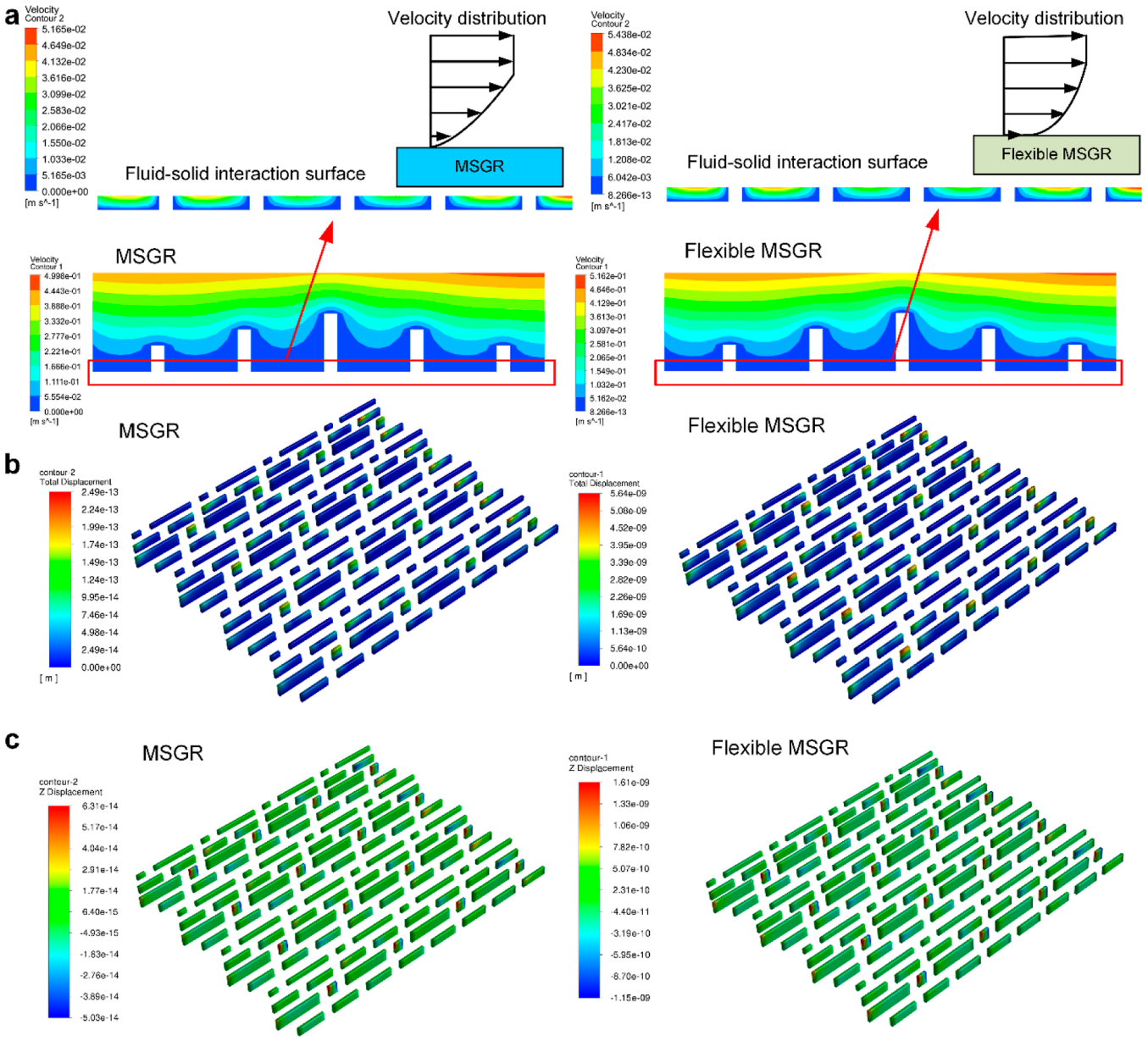

Figure 8. Velocity and displacement contours on the MSGR surface and the flexible MSGR surface. (a) Velocity contours, (b) total displacement, and (c) normal displacement on the MSGR surface and the flexible MSGR surface, where the flexible MSGR surface was made of PDMS and curing agent in the ratio of 10:1.

between the MSGR and flexible MSGR surface. When the inclination angle increased to 60°, coffee droplets on the flexible MSGR surface rolled down to the bottom of the inclined surface. The results showed that flexible MSGR surfaces had better antifouling performance than MSGR surfaces.

4. DISCUSSION

4.1. Synergistic DR Effect of the Flexible MSGR Surface. The comparison of the DR results with wettability showed no direct correlation. The MSGR surface showed a low static CA in rigid bionic surfaces but a small drag. Therefore, it is important to analyze the effect of structure and material deformation on DR. Figure 7a presents contours of constant flow velocity in a wall-parallel plane at a distance of 0.1δ from the bottom for different rigid bionic surfaces, where δ denotes the boundary layer thickness.[40] On the MSGR surface, high- and low-velocity streaks appeared near the low riblet (black arrow) and high riblet (red arrow), respectively. Similar conclusions were obtained from the study of the European bass and tuna.[40−42] More detailed information on the velocity variation in different bionic surfaces is demonstrated in Figure 7b, which exhibited spanwise velocity profiles for different wall-normal locations at the location $y = y_o + 3100$ μm. Except for that of the MSGR surface, the streak amplitude of other surfaces was less than 0.07 of the inlet velocity, and no high- and low-velocity streaks were formed. For the MSGR surface, the high- and low-velocity streaks extended through most of the boundary layer at different depths. As the normal distance from the wall was lengthened, the amplitude of the streak decreased monotonically until the outer edge of the boundary layer reached zero amplitude. In order to explore the effect of high- and low-velocity streaks on DR, velocity contours of the boundary layer cross-sections of the R, F, and

https://doi.org/10.1021/acsomega.2c07729
ACS Omega 2023, 8, 8569−8581

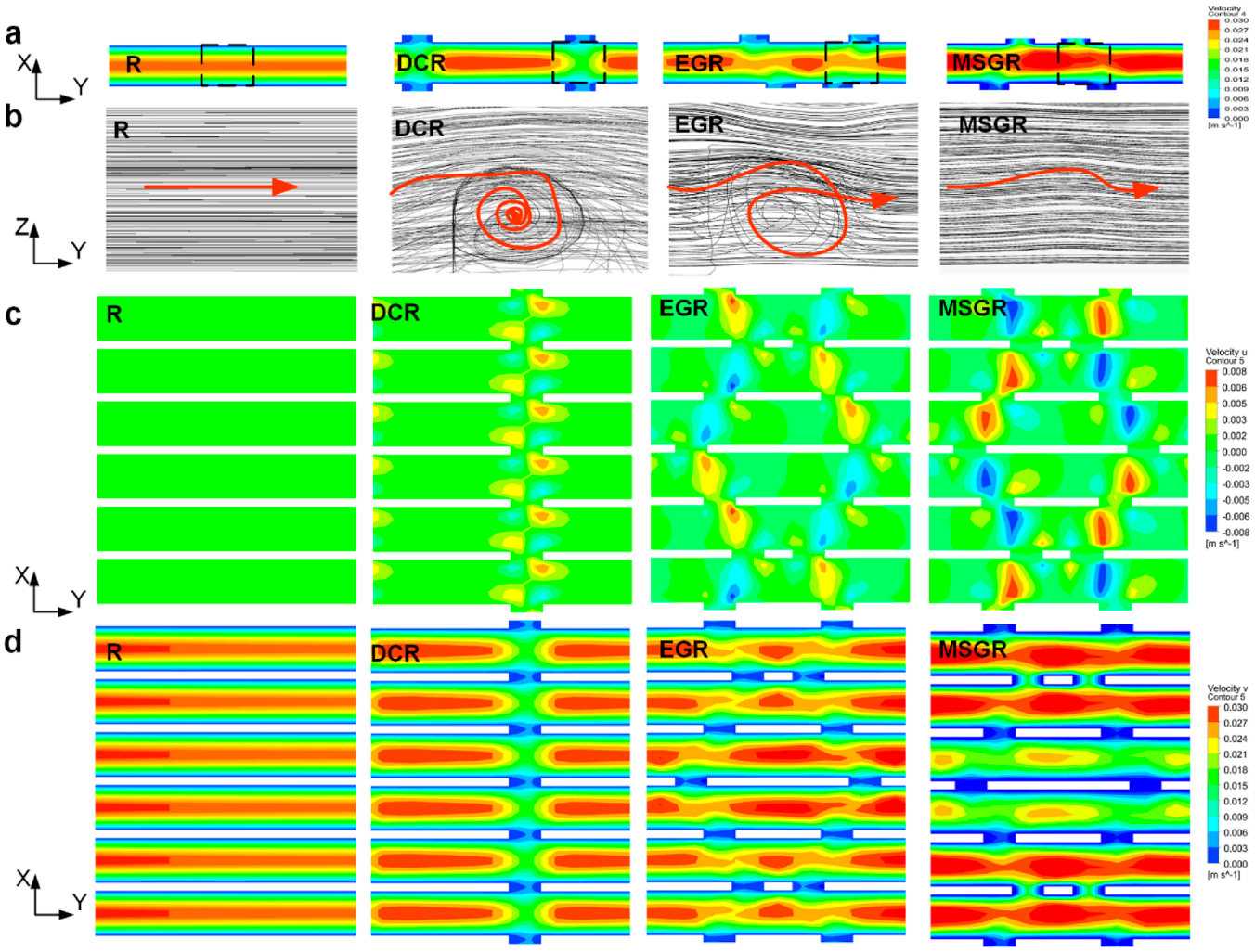

Figure 9. Velocity contours and flow fields on different rigid bionic surfaces. (a) Velocity distribution of a single riblet with a height of 0.1δ from the bottom of different bionic surfaces. (b) Path lines in $y-z$ planes in the groove region corresponding to the dashed box in (a), and the velocity distributions of (c) x- and (d) y-components at a height of 0.1δ from the bottom on different surfaces.

MSGR surfaces were analyzed, as shown in Figure 7c. Note that for each row of rhombus-shaped patterns, the results were periodic in the spanwise direction. A detailed comparison of dimensionless velocity profiles in the R surface and the high- and low-velocity regions of the MSGR surface are shown in Figure 7d. Compared with the velocity profile of the F surface (black line), the velocity gradient near the wall became flatter at points A, B, and C. However, the thickness of the boundary layer was almost consistent. This suggested that riblets changed the shape of the velocity profile in the boundary layer area but not the thickness of the boundary layer (despite affecting the near-wall flow). The near-wall flow was modulated by the MSGR surface, with streaks that would affect the wall shear stress (τ_w) distribution compared with flow over a classic single-stage riblet surface. In comparison with the velocity profile for an R surface (green line), the velocity gradient of the MSGR surface got flatter along the low-velocity area (red line) but steeper along the high-velocity area (blue line). The wall shear stress had direct relationship to the velocity gradient; thus, the wall shear stress along the span of the MSGR surface was relevant to the low- and high-velocity areas. The integral of the wall shear stress over the entire surface was the total friction drag, which was the synergistic DR effect of streaks.

In addition, the MSGR surface could be deemed to be distributed roughness on an F surface, and the roughness Reynolds number was calculated to be 55 based on $Re_k = \rho u_k h/\mu$, where u_k denoted the velocity at the peak roughness height (i.e., riblet height h_1). The critical roughness Reynolds number of induced bypass transition was approximately 250.[40] Therefore, the roughness Reynolds number was much smaller than the critical value. This suggests that MSGRs, as micro-roughness elements placed within the boundary layer, could generate stable low- and high-velocity streaks without causing bypass transitions. Taken together, the presented MSGR surface could generate steady low- and high-velocity streaks and reduce the velocity gradient in the boundary layer, thus achieving DR.

To explore why the DR effect of the flexible MSGR surface is better than that of the MSGR surface, Figure 8a shows the velocity contours of both surfaces at the same position. A small velocity was generated in the near-wall region of the flexible MSGR surface, while the fluid velocity in the near-wall region of the MSGR surface was almost 0. Velocity slips were produced in the flexible MSGR surface, which further reduced the velocity gradient in the boundary layer. In addition, the flexible MSGR surface was slightly deformed by fluid flow, as shown in Figure 8b,c. At the inlet velocity of 1 m/s, the

https://doi.org/10.1021/acsomega.2c07729
ACS Omega 2023, 8, 8569−8581

maximum deformation of the flexible MSGR surface was 5.64 × 10^{-9} m, which was significantly larger than that of the MSGR surface and effectively absorbed turbulent pulsation. Therefore, the flexible MSGR surface showed superior DR effects compared with the MSGR surface. However, greater deformation displacement did not mean better DR performance of the surface. When the deformation of the flexible riblet in the downstream and spanwise directions gradually increased, the basic shape of the riblet changed, and the DR effect diminished. The elastic modulus was an important factor in maintaining the shape, which explained why the flexible MSGR surface with an elastic modulus of 4.592 MPa had the best DR performance.

4.2. Efficient Antifouling Effect of the Flexible MSGR Surface. The attachment point theory indicated that organisms preferred to attach to shaped surfaces with more contact points,[23] which explained the difference in the attachment of organisms on different bionic surfaces in static antifouling experiments. However, the contact points of organisms on the surface were variable in dynamic testing. By predicting the physical pathway of pollutants via analyzing the flow characteristics adjacent to the various bionic surfaces, the possible antifouling performance of bionic surfaces was explained physically. Notably, the flow between protruding riblets could be divided into main and secondary streams, as shown in Figure S5. For example, in the R and EGR surfaces, the red and blue curves represented the main and secondary streams, respectively. The EGR surface with asymmetric intersections enabled the flow to partially enter or leave the riblet gap to form a secondary stream.

Figure 9a illustrates the velocity distributions of a single riblet at 0.1δ height from the bottom of different rigid bionic surfaces. Because no geometric factors interfered with the flow, the flow velocity of the main stream was uniform on the R surface. In contrast, the flow on the DCR surface was affected by small vortices, and thus, the main stream was locally decelerated, as shown by the dashed box in Figure 9a. The small vortex originated from the rotating flow of the riblet gap in the bottom pattern. In addition, the secondary stream in the EGR and MSGR surfaces caused local flow communication between adjacent grooves. The secondary stream weakened the small vortex near the riblet gap, alleviating the main stream deceleration in the groove. It was worth noting that the flow velocity of the main stream on the MSGR surface was much more uniform than that on the EGR surface, which might be because almost no isolated rotating vortex existed in the groove of the MSGR surface, as shown in Figure 9b. Figure 9c presents the velocity distributions of the x-component at 0.1δ height from the bottom of different rigid bionic surfaces. The flow velocity in the groove was similar, but a slight difference was observed near the riblet gap. The secondary stream was observed near the riblet gap on the MSGR and EGR surfaces but not on the R and DCR surfaces. The secondary stream on the MSGR surface was significantly stronger than that on the EGR surface, leading to almost no vortex near the riblet gap; the main stream velocity in the groove was more uniform. As shown in Figure 9d, due to the high- and low-velocity streaks in the MSGR surface, the secondary stream was enhanced, and the residence time of pollutants was shortened. In detail, the secondary stream could pass through the riblet gap inward and outward, breaking the isolated rotating vortex in the groove and reducing the residence time of pollutants at the bottom. In addition, high- and low-velocity streaks on the MSGR surface could reduce the selectivity of pollutants, namely, the synergistic antifouling effect of streaks.

Compared with the MSGR surface, the flexible MSGR surface had certain hydrophobicity and lower surface energy, which improved its adhesion resistance and further enhanced its antifouling performance.

5. CONCLUSIONS

Flexible MSGRs was proposed to improve DR and antifouling ability by the optimization of the near-wall velocity distribution. Experimental and numerical simulation methods were performed to characterize the DR and antifouling effects of the flexible MSGR surface. According to the analysis of the circulating water tunnel, flexible MSGRs could accomplish greater DR than the classic single-stage riblet with uniform parameters and expand the effective DR speed range. In addition, computational fluid dynamics was used to analyze the flow on the flexible MSGR surface, which identified that high- and low-velocity streaks alternated along the span. This regular arrangement of streaky structures could bring about changes in the flow near the wall, velocity gradient reduction of the boundary layer, and further DR. Moreover, the elastic modulus of the flexible MSGR surface with the best DR effect was 4.592 MPa, which could produce velocity slip, further reduce the velocity gradient of the boundary layer, and absorb pressure fluctuations, thus achieving a DR rate of 16.8% at a flow rate of 0.5 m/s. Flexible MSGRs, serving as an antifouling microstructure, could reduce the adhesion coefficient of *C. vulgaris* by about 69.6% compared with an F surface. The secondary stream and high- and low-velocity streaks were generated in the low surface energy flexible MSGR surface with asymmetric intersection and high- and low-gradient riblet, breaking the isolated rotating vortex in the groove, shortening the residence time of pollutants, reducing the selectivity of pollutants, and enhancing the anti-adhesion property. In summary, flexible MSGRs provide a feasible solution for ship DR and pollution prevention.

■ ASSOCIATED CONTENT

Supporting Information

The Supporting Information is available free of charge at https://pubs.acs.org/doi/10.1021/acsomega.2c07729.

Preparation of the flexible MSGR surface, schematic diagram of the computational domain and the entrance grids of the MSGR surface, sliding angle of different bionic surfaces, antifouling test results of *C. vulgaris* on different bionic surfaces, and representative flow characteristics of the R surface and EGR surface (PDF)

■ AUTHOR INFORMATION

Corresponding Author

Huawei Chen − *School of Mechanical Engineering and Automation, Beihang University, Beijing 100191, China; Advanced Innovation Center for Biomedical Engineering, Beihang University, Beijing 100191, China*; Email: chenhw75@buaa.edu.cn

Authors

Xianxian Cui − *School of Mechanical Engineering and Automation, Beihang University, Beijing 100191, China*; orcid.org/0000-0002-3327-5612

https://doi.org/10.1021/acsomega.2c07729
ACS Omega 2023, 8, 8569−8581

Dengke Chen − *School of Transportation, Ludong University, Yantai 264025 Shandong Province, China;* orcid.org/0000-0002-2383-648X

Complete contact information is available at: https://pubs.acs.org/10.1021/acsomega.2c07729

Notes

The authors declare no competing financial interest.

■ ACKNOWLEDGMENTS

This work was supported by the National Natural Science Foundation of China (grant nos. 51935001, 51725501, T2121003, and 51905022) and the National Key R&D Program of China (grant no. 2019YFB1309702).

■ REFERENCES

(1) Ko, Y. S.; Kim, H. J.; Ha, C. W.; Lee, C. Quantifying Frictional Drag Reduction Properties of Superhydrophobic Metal Oxide Nanostructures. *Langmuir* **2020**, *36*, 11809−11816.
(2) Bixler, G. D.; Bhushan, B. Fluid Drag Reduction with Shark-Skin Riblet Inspired Microstructured Surfaces. *Adv. Funct. Mater.* **2013**, *23*, 4507−4528.
(3) Liu, M.; Ma, L. Drag reduction methods at solid-liquid interfaces. *Friction* **2021**, *10*, 491−515.
(4) Tian, G.; Fan, D.; Feng, X.; Zhou, H. Thriving artificial underwater drag-reduction materials inspired from aquatic animals: progresses and challenges. *RSC Adv.* **2021**, *11*, 3399−3428.
(5) Wu, L.; Wang, H.; Song, Y.; Zhang, B.; Xu, Y.; Liu, C.; Yan, Y. Drag reduction mechanism of Paramisgurnus dabryanus loach with self-lubricating and flexible micro-morphology. *Sci. Rep.* **2020**, *10*, 12873.
(6) Cai, Y.; Lin, L.; Xue, Z.; Liu, M.; Wang, S.; Jiang, L. Filefish-Inspired Surface Design for Anisotropic Underwater Oleophobicity. *Adv. Funct. Mater.* **2014**, *24*, 809−816.
(7) Seo, D.; Cha, S. K.; Kim, G.; Shin, H.; Hong, S.; Cho, Y. H.; Chun, H.; Choi, Y. Flexible and Stable Omniphobic Surfaces Based on Biomimetic Repulsive Air-Spring Structures. *ACS Appl. Mater. Interfaces* **2019**, *11*, 5877−5884.
(8) Yunqing, G.; Tao, L.; Jiegang, M.; Zhengzan, S.; Peijian, Z. Analysis of Drag Reduction Methods and Mechanisms of Turbulent. *Appl. Bionics Biomech.* **2017**, *2017*, 6858720.
(9) Li, Y.; Yin, K.; Diao, Y.; Fang, M.; Yang, J.; Zhang, J.; Cao, H.; Liu, X.; Jiang, J. A biopolymer-gated ionotronic junctionless oxide transistor array for spatiotemporal pain-perception emulation in nociceptor network. *Nanoscale* **2022**, *14*, 2316−2326.
(10) Bixler, G. D.; Bhushan, B. Shark skin inspired low-drag microstructured surfaces in closed channel flow. *J. Colloid Interface Sci.* **2013**, *393*, 384−396.
(11) Han, X.; Zhang, D.; Li, X.; Li, Y. Bio-replicated forming of the biomimetic drag-reducing surfaces in large area based on shark skin. *Sci. Bull.* **2008**, *53*, 1587−1592.
(12) Chen, H.; Zhang, X.; Ma, L.; Che, D.; Zhang, D.; Sudarshan, T. S. Investigation on large-area fabrication of vivid shark skin with superior surface functions. *Appl. Surf. Sci.* **2014**, *316*, 124−131.
(13) Wen, L.; Weaver, J. C.; Lauder, G. V. Biomimetic shark skin: design, fabrication and hydrodynamic function. *J. Exp. Biol.* **2014**, *217*, 1656−1666.
(14) Zhang, D.; Luo, Y.; Li, X.; Chen, H. Numerical Simulation and Experimental Study of Drag-Reducing Surface of a Real Shark Skin. *J. Hydrodyn.* **2011**, *23*, 204−211.
(15) Dundar Arisoy, F.; Kolewe, K. W.; Homyak, B.; Kurtz, I. S.; Schiffman, J. D.; Watkins, J. J. Bioinspired Photocatalytic Shark-Skin Surfaces with Antibacterial and Antifouling Activity via Nanoimprint Lithography. *ACS Appl. Mater. Interfaces* **2018**, *10*, 20055−20063.
(16) Boomsma, A.; Sotiropoulos, F. Direct numerical simulation of sharkskin denticles in turbulent channel flow. *Phys. Fluids* **2016**, *28*, 035106.
(17) Jung, Y. C.; Bhushan, B. Biomimetic structures for fluid drag reduction in laminar and turbulent flows. *J. Phys.: Condens. Matter* **2010**, *22*, 035104.
(18) Mohammadi, A.; Floryan, J. M. Numerical Analysis of Laminar-Drag-Reducing Grooves. *J. Fluids Eng.* **2015**, *137*, 041201.
(19) Mohammadi, A.; Floryan, J. M. Groove optimization for drag reduction. *Phys. Fluids* **2013**, *25*, 113601.
(20) Zhou, Z.; Wang, S.; Yan, Z.; Wang, D.; Deng, J.; He, Y.; Yuan, W. Low Air Drag Surface via Multilayer Hierarchical Riblets. *ACS Appl. Mater. Interfaces* **2021**, *13*, 53155−53161.
(21) Schumacher, J. F.; Aldred, N.; Callow, M. E.; Finlay, J. A.; Callow, J. A.; Clare, A. S.; Brennan, A. B. Species-specific engineered antifouling topographies: correlations between the settlement of algal zoospores and barnacle cyprids. *Biofouling* **2007**, *23*, 307−317.
(22) Dai, W.; Alkahtani, M.; Hemmer, P. R.; Liang, H. Drag-reduction of 3D printed shark-skin-like surfaces. *Friction* **2018**, *7*, 603−612.
(23) Qin, L.; Ma, Z.; Sun, H.; Lu, S.; Zeng, Q.; Zhang, Y.; Dong, G. Drag reduction and antifouling properties of non-smooth surfaces modified with ZIF-67. *Surf. Coat. Technol.* **2021**, *427*, 127836.
(24) Zhou, Z.; Yan, Z.; Zhang, K.; Zhou, W.; Ou, Z.; Lv, X.; He, Y.; Yuan, W. Bioinspired drag reduction surfaces via triple lithography method based on three-layer hybrid masks. *J. Micromech. Microeng.* **2022**, *32*, 055006.
(25) Chen, D.; Cui, X.; Chen, H. Dual-composite drag-reduction surface based on the multilayered structure and mechanical properties of tuna skin. *Microsc. Res. Tech.* **2021**, *84*, 1862−1872.
(26) Kim, T.; Kwon, S.; Lee, J.; Lee, J. S.; Kang, S. A metallic anti-biofouling surface with a hierarchical topography containing nanostructures on curved micro-riblets. *Microsc. Res. Tech.* **2022**, *8*, 6.
(27) Chung, K. K.; Schumacher, J. F.; Sampson, E. M.; Burne, R. A.; Antonelli, P. J.; Brennan, A. B. Impact of engineered surface microtopography on biofilm formation of Staphylococcus aureus. *Biointerphases* **2007**, *2*, 89−94.
(28) Choi, W.; Lee, C.; Yoo, C. H.; Shin, M. G.; Lee, G. W.; Kim, T. S.; Jung, H. W.; Lee, J. S.; Lee, J. H. Structural tailoring of sharkskin-mimetic patterned reverse osmosis membranes for optimizing biofouling resistance. *J. Membr. Sci.* **2020**, *595*, 117602.
(29) Yoo, C. H.; Lee, G. W.; Choi, W.; Shin, M. G.; Lee, C.; Shin, J. H.; Son, Y.; Chun, B.; Lee, J. H.; Jung, H. W.; Lee, J. S. Identifying the colloidal fouling behavior on the sharkskin-mimetic surface: In-situ monitoring and lattice Boltzmann simulation. *Chem. Eng. J.* **2021**, *405*, 126617.
(30) Lee, C.; Lee, G. W.; Choi, W.; Yoo, C. H.; Chun, B.; Lee, J. S.; Lee, J. H.; Jung, H. W. Pattern flow dynamics over rectangular Sharklet patterned membrane surfaces. *Appl. Surf. Sci.* **2020**, *514*, 145961.
(31) Schumacher, J. F.; Long, C. J.; Callow, M. E.; Finlay, J. A.; Callow, J. A.; Brennan, A. B. Engineered Nanoforce Gradients for Inhibition of Settlement (Attachment) of Swimming Algal Spores. *Langmuir* **2008**, *24*, 4931−4937.
(32) Wu, Z.; Yin, K.; Wu, J.; Zhu, Z.; Duan, J. A.; He, J. Recent advances in femtosecond laser-structured Janus membranes with asymmetric surface wettability. *Nanoscale* **2021**, *13*, 2209−2226.
(33) Yin, K.; Wang, L.; Deng, Q.; Huang, Q.; Jiang, J.; Li, G.; He, J. Femtosecond Laser Thermal Accumulation-Triggered Micro-/Nano-structures with Patternable and Controllable Wettability Towards Liquid Manipulating. *Nano-Micro Lett.* **2022**, *14*, 97.
(34) Li, X.; Cai, J.; Zhang, D. Y. Study on the Manufacturing Method of the Biomimetic Drag Reducing Morphology Replication Mold. *Adv. Mater. Res.* **2010**, *97*−*101*, 2533−2537.
(35) Domel, A. G.; Domel, G.; Weaver, J. C.; Saadat, M.; Bertoldi, K.; Lauder, G. V. Hydrodynamic properties of biomimetic shark skin: effect of denticle size and swimming speed. *Bioinspiration Biomimetics* **2018**, *13*, 056014.
(36) Jiang, P. X.; Fan, M. H.; Si, G. S.; Ren, Z. P. Thermal-hydraulic performance of small scale micro-channel and porous-media heat-exchangers. *Int. J. Heat Mass Transfer* **2001**, *44*, 1039−1051.

(37) Védie, E.; Barry-Martinet, R.; Senez, V.; Berglin, M.; Stenlund, P.; Brisset, H.; Bressy, C.; Briand, J. F. Influence of Sharklet-Inspired Micropatterned Polymers on Spatio-Temporal Variations of Marine Biofouling. *Macromol. Biosci.* **2022**, *22*, No. e2200304.
(38) Li, L.; Liu, B. .; Hao, H.; Li, L.; Zeng, Z. Investigation of the drag reduction performance of bionic flexible coating. *Phys. Fluids* **2020**, *32*, 083302.
(39) Vasudevan, R.; Kennedy, A. J.; Merritt, M.; Crocker, F. H.; Baney, R. H. Microscale patterned surfaces reduce bacterial fouling-microscopic and theoretical analysis. *Colloids Surf., B* **2014**, *117*, 225−232.
(40) Muthuramalingam, M.; Villemin, L. S.; Bruecker, C. Streak formation in flow over biomimetic fish scale arrays. *J. Exp. Biol.* **2019**, *222*, jeb205963.
(41) Muthuramalingam, M.; Puckert, D. K.; Rist, U.; Bruecker, C. Transition delay using biomimetic fish scale arrays. *Sci. Rep.* **2020**, *10*, 14534.
(42) Chen, D.; Chen, H.; Cui, X. Dual-coupling drag reduction inspired by tuna skin: Fan-shaped imbricated fish scale composited with flexible coating. *AIP Adv.* **2022**, *12*, 035218.

https://doi.org/10.1021/acsomega.2c07729
ACS Omega 2023, 8, 8569−8581